remote sensing

MDPI

Article

Assessment of Surface Inundation Monitoring and Drivers after Major Storms in a Tropical Island

Mei Yu * and Qiong Gao

Department of Environmental Sciences, University of Puerto Rico, Rio Piedras, San Juan, PR 00925, USA
* Correspondence: meiyu@ites.upr.edu

Abstract: Extreme climate events such as storms and severe droughts are becoming more frequent under the warming climate. In the tropics, excess rainfall carried by hurricanes causes massive flooding and threatens ecosystems and human society. We assessed recent major floodings on the tropical island of Puerto Rico after Hurricane Maria in 2017 and Hurricane Fiona in 2022, both of which cost billions of dollars damages to the island. We analyzed the Sentinel-1 synthetic aperture radar (SAR) images right after the hurricanes and detected surface inundation extent by applying a random forest classifier. We further explored hurricane rainfall patterns, flow accumulation, and other possible drivers of surface inundation at watershed scale and discussed the limitations. An independent validation dataset on flooding derived from high-resolution aerial images indicated a high classification accuracy with a Kappa statistic of 0.83. The total detected surface inundation amounted to 10,307 ha after Hurricane Maria and 7949 ha after Hurricane Fiona for areas with SAR images available. The inundation patterns are differentiated by the hurricane paths and associated rainfall patterns. We found that flow accumulation estimated from the interpolated Fiona rainfall highly correlated with the ground-observed stream discharges, with a Pearson's correlation coefficient of 0.98. The detected inundation extent was found to depend strongly on hurricane rainfall and topography in lowlands within watersheds. Normal climate, which connects to mean soil moisture, also contributed to the differentiated flooding extent among watersheds. The higher the accumulated Fiona rain and the lower the mean elevation in the flat lowlands, the larger the detected surface flooding extent at the watershed scale. Additionally, the drier the climate, which might indicate drier soils, the smaller the surface flooding areas. The approach used in this study is limited by the penetration capability of C-band SAR; further application of L-band images would expand the detection to flooding under dense vegetation. Detecting flooding by applying machine learning techniques to SAR satellite images provides an effective, efficient, and reliable approach to flood assessment in coastal regions on a large scale, hence helping to guide emergency responses and policy making and to mitigate flooding disasters.

Keywords: coastal inundation; SAR; machine learning; discharges; major storms; Bayesian regression kriging

check for updates

Citation: Yu, M.; Gao, Q. Assessment of Surface Inundation Monitoring and Drivers after Major Storms in a Tropical Island. *Remote Sens.* **2024**, *16*, 503. https://doi.org/10.3390/rs16030503

Academic Editor: Yuriy Kuleshov

Received: 9 December 2023
Revised: 16 January 2024
Accepted: 23 January 2024
Published: 28 January 2024

Copyright: © 2024 by the authors. Licensee MDPI, Basel, Switzerland. This article is an open access article distributed under the terms and conditions of the Creative Commons Attribution (CC BY) license (https://creativecommons.org/licenses/by/4.0/).

1. Introduction

Extreme climate events are becoming more frequent and severe under the warming climate [1], and climate models have predicted increased extreme El Niño and extreme La Niña events [2,3]. The increase in tropical cyclones, both in frequency and in intensity, and the lengthy droughts, together with heat waves, are connected to large-scale mangrove mortality globally [4,5]. Coastal regions support the highest population density, yet they are more prone than inland areas to damage by tropical storms, as the lowlands in the coast are more likely to be inundated [6,7]. In coastal regions, destructive tropical cyclones have brought disastrous damage to ecosystems and threatened dense coastal communities through events such as widespread floods resulting from heavy rainfall, coastal storm surge, and rising sea level [8–10]. The exacerbation of more frequent and intense tropical

cyclones on coastal compound flooding raises great concerns for flooding monitoring and rapid responses [11,12].

Hydrodynamic modeling and remote sensing are the main tools to assess and monitor coastal flooding [13,14]. Recent advances in remote sensing have greatly improved flooding monitoring and assessment in accuracy, spatiotemporal resolution, and timing [15,16]. More frequent and open high-resolution images such as Sentinel and Landsat images [17–19] make it possible to monitor surface inundation at greater spatial and temporal resolutions. Compared to optical sensors [14], the capability of cloud penetration by synthetic aperture radar (SAR) makes all-weather monitoring possible, thus greatly enhancing the applications of SAR in detecting surface inundation [16,20]. Furthermore, cloud computation platforms such as Google Earth Engine (GEE) [21] significantly improve the efficiency, effectiveness, and timeliness of surface inundation monitoring and assessment.

Inundated pixels are usually detected from remote sensing images by local or global threshold of signals or their statistics [16,22], change detection between flooding and non-flooding periods [23–26], and supervised or unsupervised classification [9,20]. Due to low signals from the water surface, global and local threshold methods are effective, efficient, and widely applied to detect water pixels by examining histograms of signals from water and non-water surfaces [22]. Compared to a simple backscatter threshold from one image, time series of multitemporal images help improve the accuracy of water detection by comparing the signal against historical Z-scores during reference periods [16]. Machine learning techniques are also applied to classify flooding areas in rapid flood assessment [20,27]. To fully automate the detection of flooding areas, Huang et al. used existing datasets to select training samples and applied random forests for supervised classification [27]. Unsupervised classification using deep learning methods such as convolutional neural network (CNN) has also been applied to automatic flooding mapping with a segmentation algorithm [20].

To understand mechanisms of surface inundations, hydrodynamic models and statistical models were developed to link the surface inundation extent and/or depth to potential drivers such as stream discharges, rainfall, topography, etc. [15,28,29]. MODIS-detected flooding was integrated with a flood routing model and a water balance model, and river flows appeared as a main driver to flooding [28]. In another study, the decadal MODIS-detected peak flooding areas exhibited a strong correlation (R^2 of 0.93) with ground-observed river flows [29]. However, comprehensive explorations of the roles of watershed storm rainfall, discharges, topography, and climate setting in surface inundation are still greatly needed to understand hydrodynamic watershed responses to storms in the tropics and to plan for rapid response to flooding hazard.

In this paper, we assessed the flooding extent on the tropical island of Puerto Rico after two hurricanes using SAR images and machine learning classification. We then explored the roles of storm rainfall and the associated stream discharges, topography, and climate setting in surface inundation. The results will further our understanding of the inundation mechanisms in the tropics and inform emergency responses to help mitigate the damage from coastal storms.

2. Methods

2.1. Study Areas

The tropical island of Puerto Rico, centered at 18°15′N, 66°30′W, is located between the Caribbean Sea and the middle North Atlantic Ocean, and it is prone to disturbances by tropical storms [30]. The land area amounts to almost 9000 km^2 with 180 km from east to west and 65 km from north to south (Figure 1). The prevailing easterly trade wind brings large amounts of rainfall to the windward central mountains, e.g., more than 4000 mm in annual rainfall in rainforests, and thus results in large alluvial plains on the northern coast, while the rain shadow leads to less than 1000 mm annual rainfall in southern dry forests.

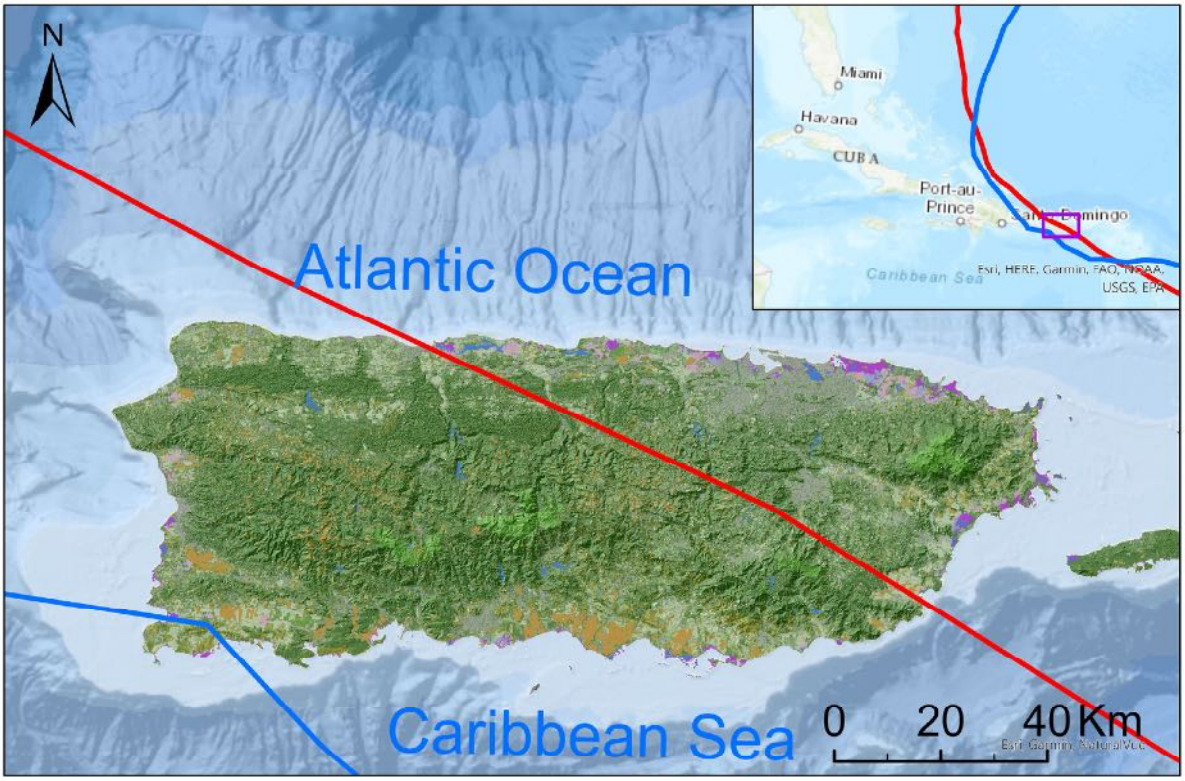

Figure 1. Topography and land cover in Puerto Rico. Hurricane paths of Maria (2017) and Fiona (2022) shown in red and blue lines, respectively. Created in ArcGIS Pro 3.2 (ESRI, Redlands, CA, USA).

Recently, Hurricane Maria and Hurricane Fiona made landfall in 2017 and 2022, respectively. Hurricane Maria brought torrential rainfall and devastating gusty winds to the island on 20 September 2017. The high-end category-four hurricane made landfall on the southeast of the island with a sustaining wind of 249 km h^{-1} and traversed the island from the southeast to the northwest (Figure 1). Hurricane rainfall was observed as high as 965 mm (38 inches), and an estimation of 1.8–2.7 m (6–9 feet) of inundation along the east coast was reported due to storm surges and tides [31]. Catastrophic flooding and flash flooding occurred during and after the storm. In 2022, Hurricane Fiona, category one, made landfall on the southwestern corner of the island on 18 September with a sustaining wind speed of 139 km h^{-1} (Figure 1). The storm surge inundation was estimated to be 0.3–0.9 m (1–3 feet) [32]. Although the wind was much less intense than that of Maria, Fiona brought heavy rains to the island, especially the southern and eastern parts. The highest storm rainfall of 823 mm (32.4 inches) was observed near Ponce in the south. Thus, some river gauges, e.g., those in Rio Grande de Loiza and Rio Grande de Manati, were reported to crest above major floods [32]. Flash floods and widespread river flooding were observed across the island. While Hurricane Maria was recorded as the costliest hurricane in Puerto Rico with $89.3 billion in damage, Hurricane Fiona was listed as the third costliest one with a damage of $2.5 billion [33].

2.2. SAR Image Analyses

We used the Google Earth Engine (GEE) [21] platform to preprocess the satellite images and further detect the surface inundation extent. The Sentinel-1 synthetic aperture radar (SAR) images [19] taken around two hurricanes and another two big rainfall events in late July 2020 and early November 2022 were used. The flooding images used were those taken on the next day after the hurricanes or the big rainfall events according to the available SAR images. For each event the reference images used are those taken in the month before or after having the same descending or ascending orbit. These

images are archived by GEE and were preprocessed for thermal noise removal, radiometric calibration, and terrain correction to a level-1 ground range detected (GRD) format (sentinel.esa.int/web/sentinel/toolboxes/sentinel-1). Backscatter intensities were converted to a backscatter coefficient (σ°) in decibels (dB) by GEE. The volume model of an angle-based radiometric slope correction, by means of a high-resolution digital elevation model (DEM, 10 m) for the island, was further applied to improve the images [34,35]. The resulted images contained the backscatter γ^0 in dB for VV (vertical transmitting with vertical receiving) and VH (vertical transmitting with horizontal receiving) bands and the layover/shadow masks [35].

We then applied a random forest classifier [36] to identify surface inundations for each flooding event [9]. Random forest classification/regression is based on the CART (classification and regression tree) algorithm, which classifies objects or regresses a dependent variable over attributes/covariates by building a hierarchical decision tree. CART works well, but it depends heavily on the selection of the training dataset and is easily overfitted with the training dataset. The random forest algorithm is designed to build multiple trees by bootstrapping into the training dataset. The final decision of classification is based on the majority of votes from all trees so that the consequence of overfit of an individual tree is avoided. For each flooding event, we created 200 trees.

The independent variables of the classification included the bands of VV, VH, the ratio of VV and VH, normalized difference flooding indices (NDFI) [24] based on VV and VH bands respectively, and the high-resolution DEM and derived slope. Backscatter values in dB were converted to natural values before calculating the indices. A reference condition was marked by the median of signals in the month before or after the flooding event. The NDFI values were calculated according to the following equations:

$$NDFI_{VV} = \frac{(VV_{ref} - VV)}{(VV_{ref} + VV)} \quad (1)$$

$$NDFI_{VH} = \frac{(VH_{ref} - VH)}{(VH_{ref} + VH)} \quad (2)$$

where VV and VH are the signals from the flooding images, and VV_{ref} and VH_{ref} are those from the reference condition.

Samples of flooding, permanent water, mangroves, herbaceous cover, forests, and urban cover were created with ground truth data, identified from high-resolution aerial photographs (Environmental Response Management Application—Caribbean, ERMA by NOAA and EPA), images during flooding and reference periods, and a high-resolution (2 m) C-CAP land-cover map from NOAA [37]. For each flooding event, 70% of samples were used for training the classifier, with the remaining for validation. For Hurricane Maria, the classifier was further rigorously validated against a separate, independent sample derived from available NOAA aerial photos (0.15 m resolution) taken right after the event [9]. Permanent water areas were further calibrated using the water bodies delineated in the USGS National Map, i.e., the areas classified as lake, pond or reservoir in the national hydrography datasets (NHD waterbody, https://apps.nationalmap.gov/downloader/#/ accessed on 10 January 2024). The accuracy of the classification was assessed with the overall accuracy, producer and user accuracies, and the Kappa statistic derived from a confusion matrix. The overall accuracy A and the Kappa statistic K were calculated as the following:

$$A = \frac{\sum_{i=1}^{n} C_{ii}}{C_{..}} \quad (3)$$

$$K = \frac{\sum_{i=1}^{n} C_{ii} - \sum_{i=1}^{n} \frac{C_{i.}C_{.i}}{C_{..}}}{C_{..} - \sum_{i=1}^{n} \frac{C_{i.}C_{.i}}{C_{..}}} \quad (4)$$

where n is the number of classes, C_{ii} is the number of samples correctly classified in the class i, $C_{..}$ is the number of total samples, and $C_{i.}$ and $C_{.i}$ are the total number of samples classified as class i and labeled as class i, respectively. Compared to the overall observed accuracy, the Kappa statistic further considers a correct classification from random chance.

We distributed the surface inundation areas to each coastal watershed using the watershed boundary (WBDHU10) delineated in the national hydrography datasets. To explore the roles of topography in surface inundation, we further analyzed the profiles of elevation as well as land cover within the detected inundation extent based on the DEM and the NOAA C-CAP land-cover map [37].

2.3. Exploration of Drivers of Surface Inundation

To further understand the drivers of surface inundation, we analyzed the hurricane rainfall pattern and the corresponding stream discharges observed during the hurricane events. Many rain gauges were damaged by the fierce wind of Hurricane Maria, and records were incomplete; thus, we chose the relatively complete rainfall records from Hurricane Fiona to conduct this analysis. Cumulative hurricane rainfall from the weather stations of NOAA (https://www.ncei.noaa.gov/cdo-web/ accessed on 21 September 2023) during the 3-day period prior to that shown in the flooding map was obtained and interpolated with the Bayesian regression kriging method (Geostatistical Analyst Module of ArcGIS Pro, version 3.0, ESRI, Redlands, CA, USA). The DEM and the distance from the hurricane path were incorporated into the regression as covariables to address their important roles in rainfall distribution [38]. As stream discharge is a key source of flood water, we obtained stream discharge in corresponding watersheds during the same period for each USGS water gauge (https://waterwatch.usgs.gov/ accessed on 10 January 2024).

After removing sinks from the DEM, we computed the flow accumulation using the Hydrology toolset for surface water (ArcGIS Pro, version 3.0, ESRI, Redlands, CA, USA). The above interpolated rainfall was used as the weight during the calculation to count the effects of the spatial heterogeneous pattern of rainfall on flow accumulation. The estimated flow accumulations were then compared to the ground-observed stream discharges to analyze their relationships using Pearson's correlation coefficient. The correlation coefficient was calculated as $r = \frac{\sum(x_i - \overline{x})\cdot(y_i - \overline{y})}{\sqrt{\sum(x_i - \overline{x})^2 \cdot \sum(y_i - \overline{y})^2}}$, where x_i and y_i are the stream discharge observed and the flow accumulation estimated at the corresponding gauge, respectively, with the mean as $\overline{x}$ and $\overline{y}$. Considering the heavy rainfall in a short time, the timing of the wet season, and the cloudy weather, we assumed that the surface stream discharges were the dominant component compared to other fluxes such as recharging soils/groundwater, evapotranspiration, and canopy interception.

Finally, we explored the potential drivers of surface inundation in coastal watersheds. We assumed that hurricane rainfall; topography, especially that of lowlands; and soil moisture status were important in determining surface inundation. We thus calculated the hurricane rainfall accumulation in each watershed by summing up the interpolated rainfall. To quantify the effect of topography in lowlands, we first chose an elevation threshold corresponding to the 70th percentile of elevation of the detected inundation pixels and defined *flat lowlands* as those areas with elevation $\leq$ the elevation threshold and slope $\leq 5°$. Then, the mean elevation of flat lowlands was calculated for each watershed as a topography index. To incorporate the sharp moisture gradient from the north to the south of the island, we assumed that the long-term mean annual rainfall highly correlated with soil moisture and could be a substitute for moisture index. Thus, we interpolated the 30-year normal annual rainfall from the NOAA weather station [38] and calculated the watershed mean of normal annual rainfall. We explored the relationship between the detected surface inundation extent and the covariates, including the watershed accumulated rainfall, the watershed topography index, and the long-term normal rainfall, by regression using R 4.2 [39].

3. Results

3.1. Detection of Surface Inundation Extent

The Sentinel-1 SAR images clearly showed low backscatter signals during flooding when compared to those in the reference period. The image from 19 September 2022 (Figure 2) showed a mean ± std of −14.3 ± 3.3 and −22.3 ± 2.9 for VV and VH, respectively, for flooding pixels, in comparison to −9.5 ± 2.5 and −15.9 ± 2.7, respectively, for them during the reference period.

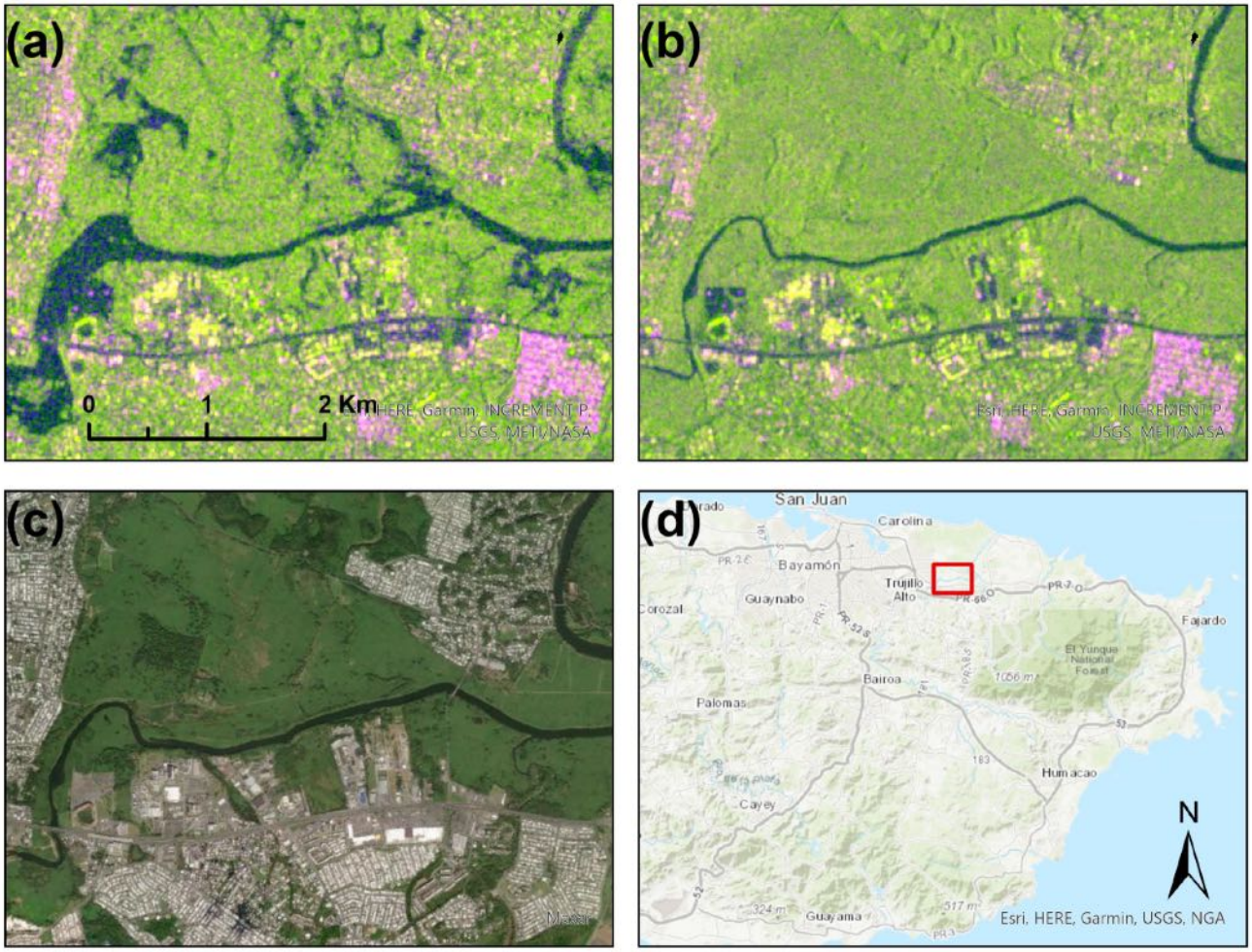

Figure 2. RGB composition of VV, VH, and their ratio from Sentinel-1 SAR on 19 September 2022 after Hurricane Fiona (**a**) and in the reference period of August 2022 (**b**). Dark blue represents water with low backscattering. High-resolution Maxar image from 8 November 2022 (**c**) and the location of the sample area (the red frame) in northeastern Puerto Rico (**d**). Created in ArcGIS Pro 3.2 (ESRI, Redlands, CA, USA).

The validation of inundation classification against the independent dataset, derived from the NOAA aerial photos (0.15 m resolution) right after Hurricane Maria, showed an overall accuracy of 0.86 and a Kappa statistic of 0.83. We adjusted the parameter of the volume correction buffer in the radiometric slope correction [35], which contributed to an improved classification accuracy compared to that of a previous application [9]. The limited canopy penetration capability of C-SAR made it difficult to detect floods under dense vegetation. Both user and producer accuracies for inundation (without dense vegetation cover) were 1, as well as those for permanent water. The user and producer accuracies are 78% and 85% for mangroves, 87% and 83% for herbaceous cover, 45% and 64% for upland forests, and 100% and 75% for urban covers, respectively. The accuracy for detecting

surface flooding pixels was high for each flooding event studied (Appendix A Classification Accuracies for Surface Inundation).

The detected surface inundation extent after Hurricane Maria in 2017 amounted to 10,307 ha, which was the greatest, followed by 7949 ha after Hurricane Fiona in 2022. The detected inundations were much less on 6 November 2022 (2338 ha) and on 31 July 2020 (2205 ha). The image coverages on these dates were the same (Appendix A). Additionally, the spatial pattern of the inundation was different between Hurricane Maria and Hurricane Fiona (Figures 3, 4 and A1). Although some watersheds such as the Cano Tiburones Coastal watershed, the Rio Cibuco watershed, and the Rio Coamo to Rio Seco watershed showed more inundation areas during Maria than during Fiona; the watersheds of Rio Grande de Manati, Rio Maunabo to Rio Humacao, and Rio Grande de Loiza exhibited more inundated areas during Fiona due to the difference in the hurricane path and associated rainfall patterns (Figure 4 and rainfall interpolation in the following section).

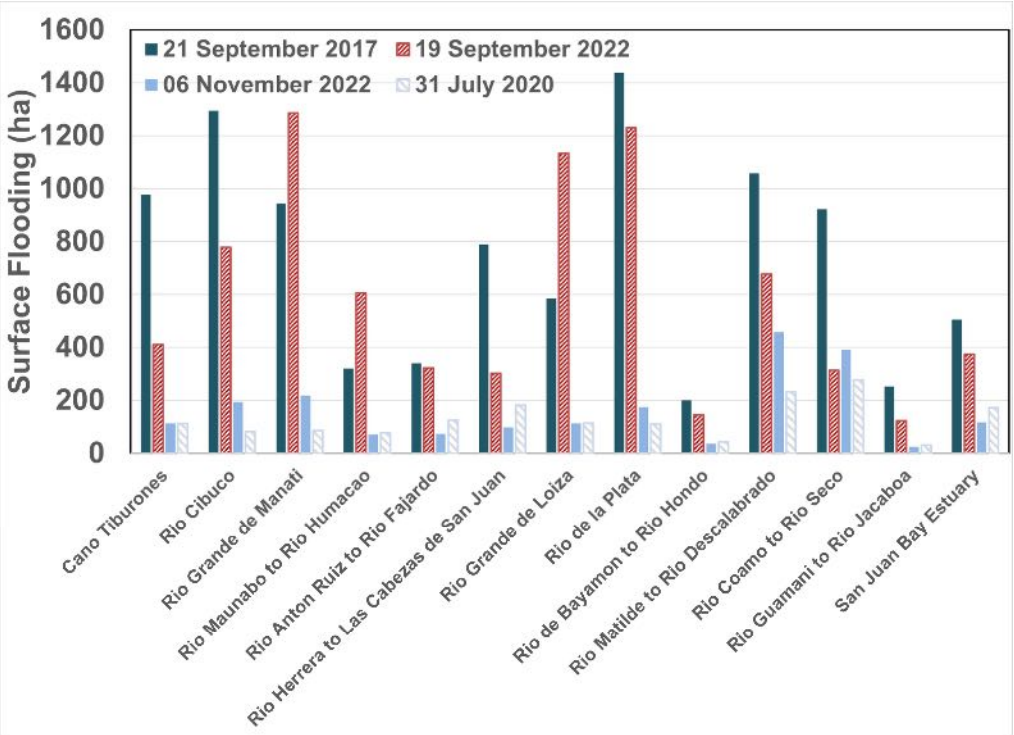

Figure 3. Surface inundation areas detected along coastal watersheds. The events on 21 September 21 2017 and 19 September 2022 correspond to the flooding after Hurricane Maria (20 September 2017) and Hurricane Fiona (18 September 2022), respectively.

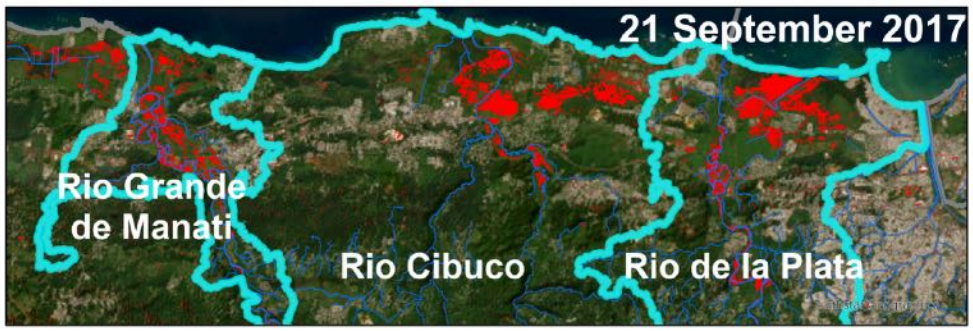

Figure 4. *Cont.*

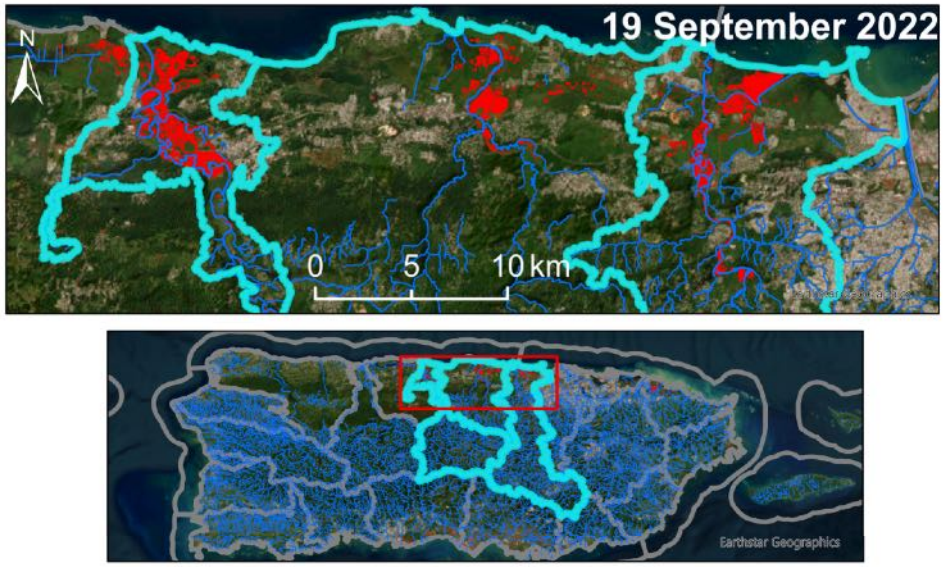

Figure 4. Detected surface inundation (red patches) on the central northern coast on 21 September 2017, right after Hurricane Maria (path shown in red), and on 19 September 2022, right after Hurricane Fiona (path shown in light blue). Blue lines are streams. Created in ArcGIS Pro 3.2 (ESRI, Redlands, CA, USA).

3.2. Topography and Land Cover in Detected Surface Inundation Areas

The profile of topography in flooded areas showed a median elevation of 8.1 m during Maria, 7.2 m during Fiona, 6.9 m on 6 November 2022, and 3.9 m on 31 July 2020. The 70th percentile of the elevation in flooded areas was 55 m during Maria and 33 m during Fiona. Both upland land covers, e.g., urban, upland herbaceous, or forest cover, and wetlands encountered large inundations during the two hurricanes (Figure 5). For most of the land-cover types, the inundation areas were larger during Maria than during Fiona, except the upland herbaceous cover, for which inundated areas represented 2897 ha during Fiona versus 2523 ha during Maria.

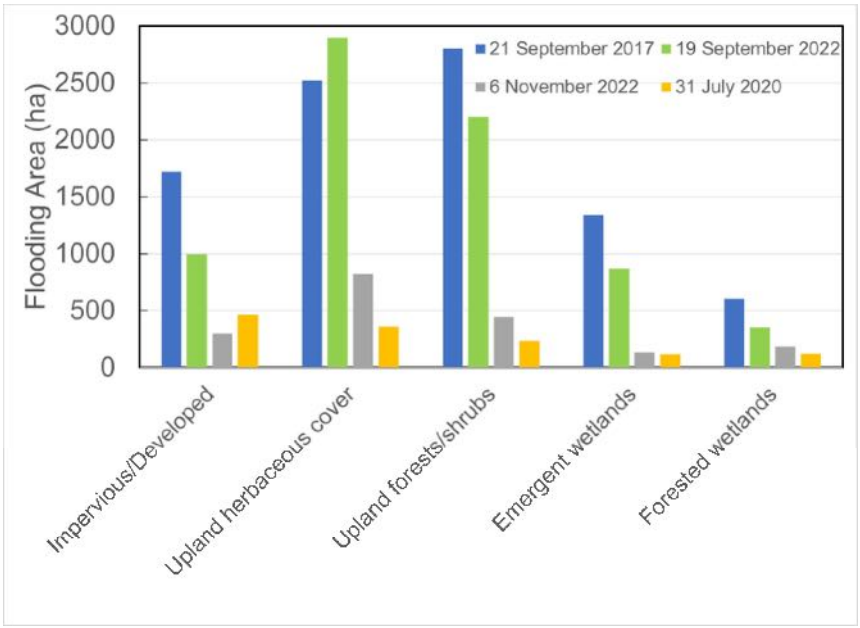

Figure 5. Detected surface inundation extent within upland and wetland land-cover zones. The events on 21 September 2017 and 19 September 2022 correspond to the flooding after Hurricane Maria and Hurricane Fiona, respectively.

3.3. Fiona Rainfall Interpolation and Flow Accumulation Compared to Observed Stream Discharge

The spatial interpolation of 3-day rainfall from Hurricane Fiona (Figure 6) resulted in a root-mean-square error (RMSE) of 78 mm, a mean standardized value of 0.005, an average standard error of 81 mm, and a root-mean-square standardized error (0.97) approaching 1. In comparison, without covariates of elevation and distance from the hurricane path the Bayesian kriging generated an interpolated rainfall pattern with an RMSE of 101 mm and an average standard error of 104 mm.

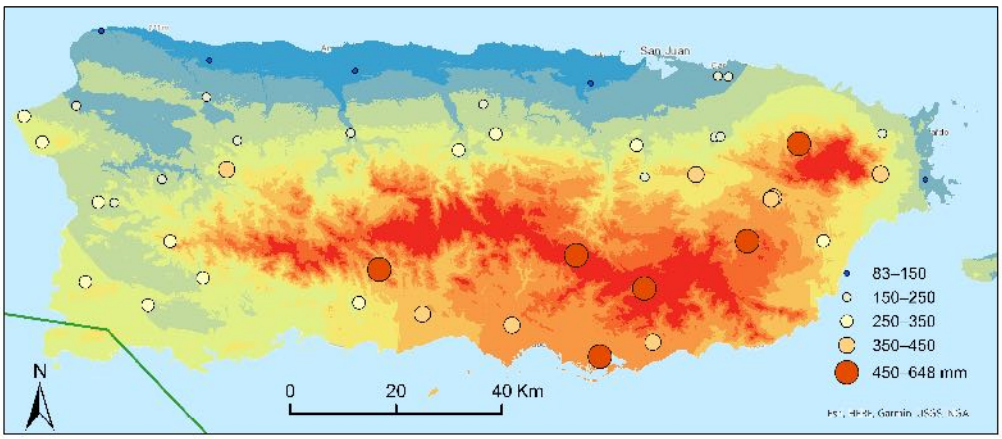

Figure 6. Fiona rainfall interpolation using Bayesian regression kriging with the covariates of DEM and distance from the hurricane path (blue line). Created in ArcGIS Pro 3.2 (ESRI, Redlands, CA, USA).

The weighted flow accumulation from the interpolated Fiona rainfall revealed a very high correlation with the ground-observed stream discharge (Figure 7). In general, the weighted flow accumulation was higher than and increased with the corresponding observation of stream discharge, and the Pearson correlation coefficient between the two was 0.98. The discharge observed at the Rio Guanajibo NR Hormigueros in the southwest was high, i.e., 160.6 Mton (Figure 7, the largest dot in the southwest on the map and the orange dot on the lower right in the plot). However, the available observations of Fiona rainfall in this area were not very high, i.e., in the range of 250–350 mm (Figure 6). Therefore, the estimated flow accumulation weighted by the rainfall was lower when compared to the observed discharge at this location (Figure 7 plot). The upstream areas of Rio Grande de Manati, Rio de la Plata, and Rio Grande de Loiza (A–C in Figure 7 Map) received huge amounts of hurricane rainfall, and the observations from downstream gauges showed large stream discharges (Figure 7, the biggest dots on the map, except the one in the southwest).

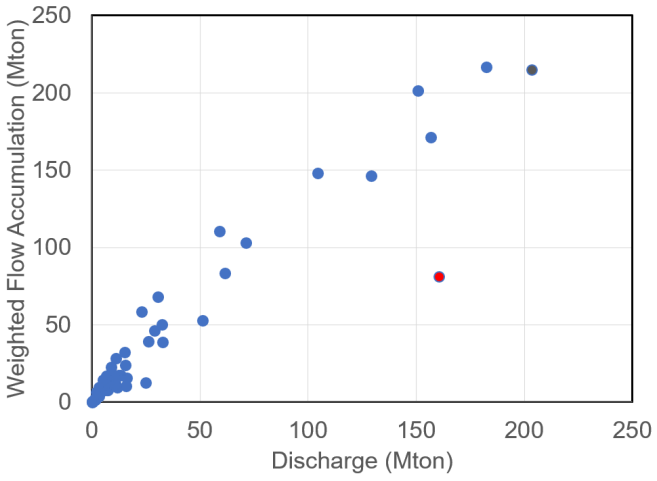

Figure 7. *Cont.*

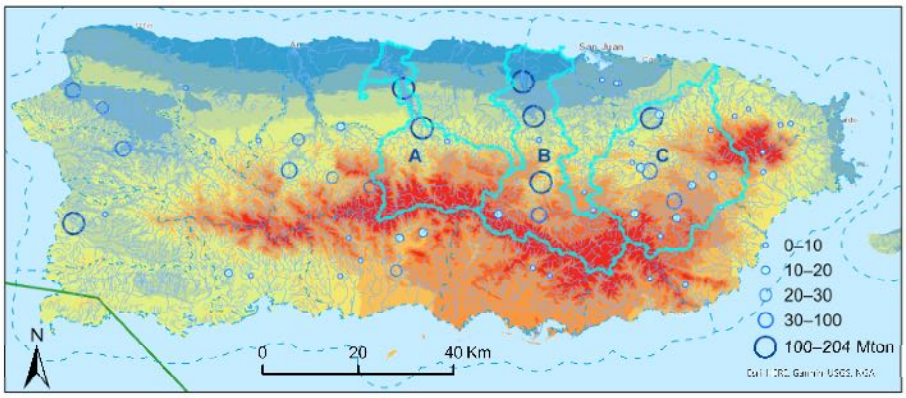

Figure 7. Ground-observed stream discharge during Hurricane Fiona versus the flow accumulation estimation weighted by Fiona rainfall (**upper panel**); spatial distribution of the observed stream discharges (dots) during Hurricane Fiona, shown on the interpolated Fiona rainfall map (**lower panel**). The dashed polygons show the watershed boundaries from USGS. A. Rio Grande de Manati watershed, B. Rio de la Plata watershed, and C. Rio Grande de Loiza watershed. Map created in ArcGIS Pro 3.2 (ESRI, Redlands, CA, USA).

3.4. Exploration of Potential Drivers to Surface Inundation

The detected surface flooding extents were highly and significantly correlated with the accumulated Fiona rain received in the watersheds (Pearson's correlation coefficient 0.59, $p = 0.04$). According to the topography of detected flooding pixels, the elevation of 33 m corresponds to 70th percentile of that in flooding pixels during Fiona. Regarding the flat lowlands in each watershed, i.e., areas with elevation $\leq$ 33 m and slope $\leq 5°$, larger flat lowlands corresponded to lower mean slope (Pearson's correlation coefficient -0.72, $p = 0.008$) and lower mean elevation (Pearson's correlation coefficient -0.44, $p = 0.15$). The mean elevation of the flat lowlands was significantly correlated with the mean slope (Pearson's correlation coefficient 0.57, $p = 0.05$).

The Fiona rain accumulated in each watershed alone could explain 35% of the variation in the surface flooding extent detected in each watershed. When it was combined with the topography index, i.e., the mean elevation of flat lowlands (DEM $\leq$ 33 m and slope $\leq 5°$), together they could explain 50% of the variation in the surface flooding extent with a p value of 0.04 for the regression. The higher the accumulated Fiona rain and the lower the flat lowlands, the larger the surface flooding extent detected (Equation (5)).

$$Flooding = 0.34 + 0.58\ Rain_{Accum} - 0.48\ DEM_{Lowland} \quad (5)$$

where $Flooding$ is the surface inundation extent in hectare, $Rain_{Accum}$ is the Fiona rain accumulation in each watershed in million tons, and $DEM_{Lowland}$ is the mean elevation of flat lowlands in m. All the variables are standardized. The p value for the coefficient before $Rain_{Accum}$ and $DEM_{Lowland}$ is 0.04 and 0.14, respectively.

The two southern watersheds, i.e., Rio Matilde to Rio Descalabrado and Rio Coamo to Rio Seco, are close to the Fiona path and encountered high Fiona rain; however, both watersheds showed relatively small inundation extents (Figure 8 upper panel). Climate in the south of the island is usually much drier than that in the east and the north due to the rain shadow effect of northeasterly trade winds [40]. When we applied normal annual rainfall in the past 30 years [38] as an additional explanatory variable, the three independent variables altogether explained 54.5% of the variation in surface flooding extent, with a p value of 0.08 for the regression (Equation (6)). Additionally, the lower the normal rainfall, that is, the drier the region, the smaller the surface flooding extent (Equation (6)).

$$Flooding = 0.11 + 0.68\ Rain_{Accum} - 0.41\ DEM_{Lowland} + 0.3\ Rain_{Normal} \quad (6)$$

where $Rain_{Normal}$ is standardized mean normal annual rainfall in mm for the watersheds. The p value for the coefficient before $Rain_{Accum}$, $DEM_{Lowland}$, and $Rain_{Normal}$ is 0.04, 0.22, and 0.40, respectively. The coefficients in front of the independent variables indicate the rank of impacts, i.e., the watershed accumulated Fiona rainfall had the largest impact (positive), followed by the mean elevation of flat lowlands (negative) and the normal annual rainfall (positive).

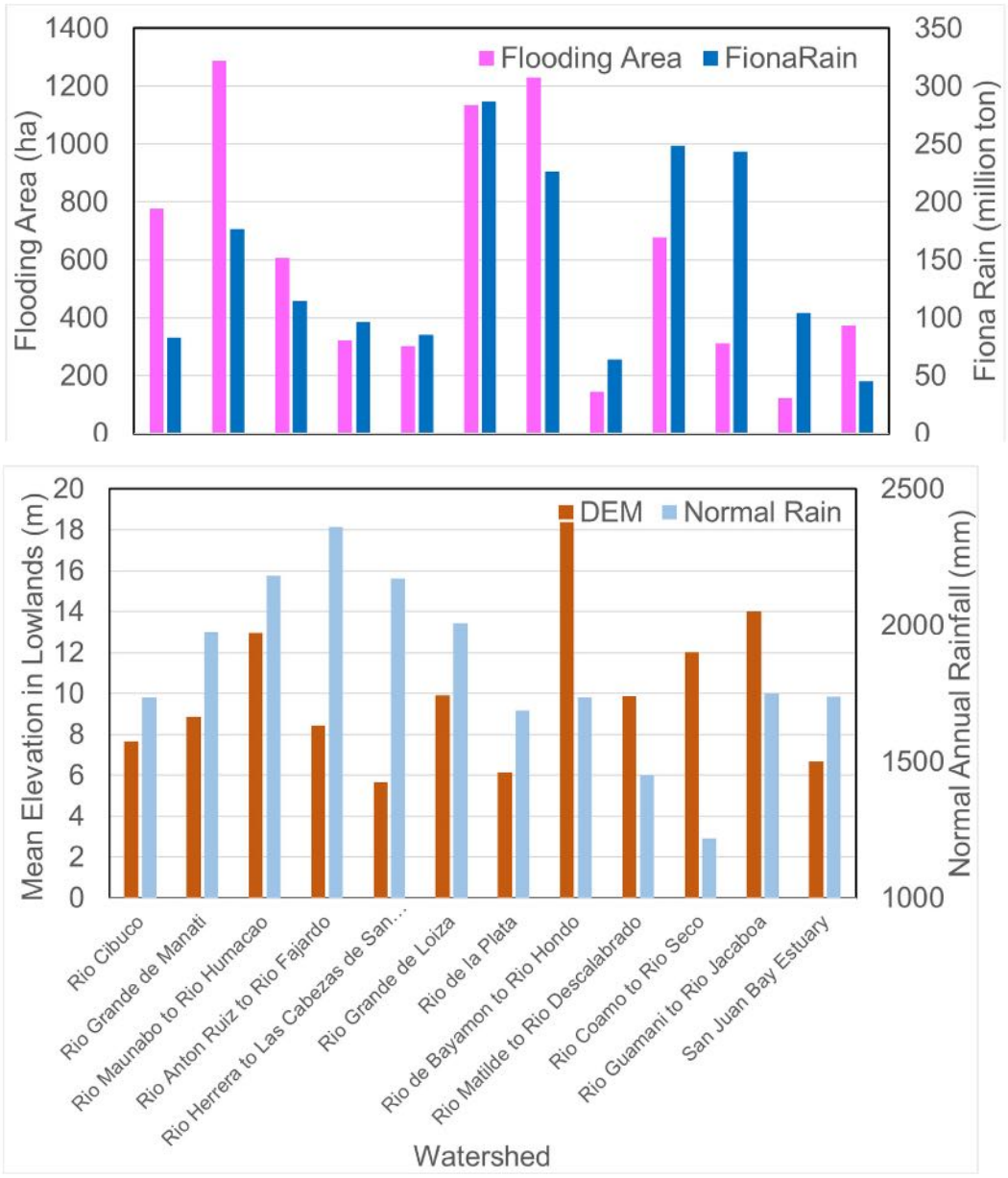

Figure 8. Detected flooding area and watershed accumulated Fiona rainfall (**upper panel**); mean elevation of flat lowlands (DEM $\leq$ 33 m and slope $\leq$ 5°) and normal annual rainfall (**lower panel**) in the coastal watersheds.

4. Discussion

The surface inundation extent after tropical storms could be detected with high accuracy when applying a machine learning algorithm to SAR images. The supervised random forest classifier applied in this study showed a Kappa statistic of 0.83 after Hurricane Maria, and the producer and the user accuracies for flooding pixels were higher than 95%. Based on a convolutional neural network (CNN) and a segmentation algorithm, Jiang et al. ap-

plied an unsupervised machine learning approach to assess large-scale flooding during the Yangtze River flood in 2020. And the results showed 93% and 94% for producer and user accuracy, respectively [20], similar to the values in this study. Under the fast development of deep learning algorithms, more applications of deep learning with SAR images have appeared for terrain surface classification, as well as other fields such as object detection, SAR-optical data fusion, etc. [41].

The C-Band SAR onboard Sentinel-1 has limited capability to detect floods under canopies [24,42]. We tried to estimate the omission of flooding under dense vegetation by exploring the depressions with forests and the nearby detected flooding pixels. However, the approach came with large uncertainties since half of these depressions only had one or two flooding pixels detected, which made it difficult to set up a reliable elevation threshold for potential flooding. An alternative would be applications of L-band images from PALSAR (phased array L-band synthetic aperture radar) and to-be-launched NISAR (NASA-ISRO synthetic aperture radar), which will largely compensate for C-band images to monitor surface floodings under canopies.

Torrential rain brought by major hurricanes, one of the major concerns of hurricane impact other than fierce wind, often leads to pluvial as well as fluvial floods. The interpolation of hurricane rainfall by Bayesian regression kriging in this study resulted in a low RMSE when elevation and distance from the hurricane path were incorporated as covariates. In general, the higher the elevation and the closer to the hurricane path, the greater the rainfall. The rainfall-derived flow accumulations are expected to be higher than the observed stream discharges since other fluxes such as recharging soils/groundwater, evapotranspiration, and canopy interception are not considered in the flow accumulation estimation. Considering the rapid heavy rainfall and cloudy weather during hurricane events, stream discharge might become the dominant component and exhibit a close correlation with the rainfall-derived flow accumulation. In this study, the flow accumulation was highly correlated with the ground-observed stream discharge during Fiona (0.98), implying not only a reliable interpolation of Fiona rainfall but also the possibility of using the interpolated rainfall in exploring drivers of surface inundation.

Remote-sensed surface inundation extents have been reported to be correlated with stream gauged discharges in existing studies [14,15,43]. For example, Frazier and Page [44] tried to relate wetland inundation extent to river flows using Landsat ETM images before and after a flooding event. In this study, the accumulated watershed Fiona rainfall played a significant role in determining the detected surface inundation extent and alone explained 35% of the variation in detected surface inundation. Heimhuber et al. [15] modeled Landsat-derived surface water inundation and tried to connect it to the lagged surface water inundation, stream discharge, local precipitation, evapotranspiration, and soil moisture. They found an average r^2 value of 0.65 for floodplain units that connected to river gauges, and stream flows dominated in the explanation of surface water inundation dynamics.

Inundation patterns are related to the distance from the hurricane path and the direction since they partly determine the consequent rainfall distribution. Hurricane winds are usually higher in areas on the right side of the path in the northern hemisphere [38,45]. As shown in Figures 3 and 4, the watershed of Rio Cibuco is mostly on the near right side of the Maria path and thus experienced more impacts from Maria and, consequently, more inundated areas compared to those during Fiona. Regarding the watershed of Rio Grande de Manati, most of its upstream area is on the left side of the Maria path, but on the right side of the Fiona path, and consequently it experienced severer inundation during Fiona than during Maria. The watershed of Rio de la Plata is among the biggest watersheds in Puerto Rico, with an area of 62,472 ha, and was approximately cut down the middle by the path of Maria. Therefore, the watershed experienced severe inundation during both hurricanes (Figure 3, the highest during Maria and the second highest during Fiona).

Topography also plays an important role in inundation. The median elevation of the detected inundation areas increased with the severity of the flooding event, e.g., 8.1 m during Maria versus 7.2 m during Fiona. Although herbaceous wetlands only occupy 1.5%

of the study area, the detected inundation in the herbaceous wetlands occupied 13% of the total inundation extent during Maria and 11% during Fiona due to their lowland settings. In the watershed of Rio Cibuco, although the accumulated Fiona rain was low, a great amount of inundated area was still observed due to its low elevation setting (Figure 8). An opposite case is the watershed of Rio de Bayamon to Rio Hondo with a relatively small inundation extent due to higher mean lowland elevation (Figure 8). The incorporation of the lowland elevation as an explanatory variable into the regression increased the explanatory capability of surface inundation extent from 35%, when considering Fiona rainfall alone, to 50%. The case here implies that the lower the flat lowland, which might also come with an increase in area, the larger the detected surface inundation extent.

Interactions between surface water and groundwater and pre-flooding soil moisture status are important in determining flooding extent and depth; however, these are less studied in the literature on flooding monitoring and modeling [13]. Our results for the potential drivers of flooding extent indirectly addressed the latter by incorporating the normal climate index. The drier the site, which might come with less antecedent soil moisture before the flooding event, the smaller the detected inundation areas. In general, the soil moisture is less saturated at drier sites in the south of the island, which may be a reason for the low inundation detected in the watershed of Rio Coamo to Rio Seco in the south. This watershed received very high amounts of Fiona rainfall (Figure 8), but since it is the driest site, the recharge of dry soils might have greatly reduced the flooding potential. Further studies incorporating the interactions between surface and groundwater are needed, especially in the Karst regions.

Our study on the hurricane impact on a tropical mountainous island thus highlights that accumulated watershed rainfall amount and topography, especially that in the lowland, dominate over other factors affecting the flooding risk; soil moisture and storm surge may also contribute to potential inundation [15,28]. The prediction of more frequent and severer tropical storms together with the trends of rapid intensification [46] raise great concerns regarding coastal flooding risk and rapid response [12]. The integration of machine learning algorithms and SAR images from cloud-computing platforms such as Google Earth Engine therefore provides an efficient, effective approach to rapid flood monitoring and response, post-disaster assessment, and the calibration/validation of hydrodynamic models for future prediction.

5. Conclusions

Coastal flooding is a major threat to the dense populations living on the coast. Under the warming climate, the rising sea level due to ocean thermal expansion and the melting of glaciers and sea ice and the increasing extreme climate events, especially the more frequent and intense tropical cyclones, exacerbate the coastal compound flooding from heavy rainfall, storm surges, and high tides. The rapid assessment and monitoring of coastal flooding are imperatives for emergency response and coastal hazard mitigation.

Advances in remote sensing, machine learning, and cloud computation greatly improve flooding assessment in terms of all-weather monitoring, accuracy, and efficiency. Using the cloud-computing platform Google Earth Engine, we assessed the surface flooding patterns on the tropical island of Puerto Rico after the high-end category 4 Hurricane Maria in 2017 and the category 1 Hurricane Fiona in 2022. We applied a random forest classifier to Sentinel-1 SAR images, for which the signals could penetrate clouds during hurricanes. To advance our mechanistic understanding of surface inundation, we interpolated the observed Fiona rainfall by Bayesian regression kriging and compared the rainfall-derived flow accumulation against the ground-observed stream discharge. Furthermore, we explored the potential drivers of surface inundation such as hurricane rainfall, stream discharge, topography, and climate setting.

In areas without dense vegetation cover, this approach could achieve high accuracy in distinguishing flooding pixels from non-flooding ones. The spatial patterns of the surface inundation after the two hurricanes are differentiated by the hurricane paths and the

associated rainfall patterns. After elevation and distance from the hurricane path were incorporated as covariates in the Bayesian regression kriging, the interpolated Fiona rainfall showed a low RMSE. And the rainfall-derived flow accumulations exhibited high correlations with the ground-observed stream discharges, which indicates a reliable interpolation approach and a possibility of using rainfall directly in exploring the drivers of surface inundation. The watershed accumulated Fiona rainfall and the watershed topography in lowlands played important roles in determining the surface flooding detected. The higher the accumulated Fiona rain and the lower the flat lowlands, the greater the detected surface inundation. Additionally, the drier the watershed, the lower the detected surface inundation.

The canopy penetration capability of C-band SAR limits the detection of flooding under dense vegetations. Future applications of L-band SAR images would largely compensate for C-SAR in monitoring the flooding with or without dense vegetation cover. The surface flooding assessment and the exploration of drivers in this study would contribute to the future integration of remote-sensed inundation with hydrological models to predict flood risk under intensified storm scenarios.

Author Contributions: Conceptualization, M.Y. and Q.G.; methodology, M.Y.; formal analysis, M.Y. and Q.G.; writing—original draft preparation, M.Y.; writing—review and editing, M.Y. and Q.G. All authors have read and agreed to the published version of the manuscript.

Funding: This research was funded by the NOAA Puerto Rico Sea Grant NA18OAR4170089.

Data Availability Statement: The datasets used are publicly available at the NOAA data portal at https://www.ncei.noaa.gov/cdo-web/ (accessed on 10 January 2024) and at https://coast.noaa.gov/dataviewer/#/ (accessed on 10 January 2024) and the USGS data portal at https://waterwatch.usgs.gov/ (accessed on 10 January 2024). Satellite Images are publicly available at Google Earth Engine.

Conflicts of Interest: The authors declare no conflicts of interest. The funders had no role in the design of the study; in the collection, analyses, or interpretation of data; in the writing of the manuscript; or in the decision to publish the results.

Appendix A Classification Accuracies for Surface Inundation

Table A1. Confusion matrix for the classification on 21 September 2017 using an independent validation sample.

	Permanent Water	Flooding	Mangroves	Herbaceous Cover	Forests	Urban	Producer Accuracy
Permanent Water	30	0	0	0	0	0	1
Flooding	0	26	0	0	0	0	1
Mangroves	0	0	29	2	3	0	0.85
Herbaceous Cover	0	0	5	45	4	0	0.83
Forests	0	0	2	3	9	0	0.64
Urban	0	0	1	2	4	21	0.75
User Accuracy	1	1	0.78	0.87	0.45	1	

Table A2. Classification results for the storms studied.

Date	Kappa	User Accuracy for Flooding	Producer Accuracy for Flooding	Overall Accuracy	SAR Image Coverage
21 September 2017 (Maria, independent validation)	0.83	1	1	0.86	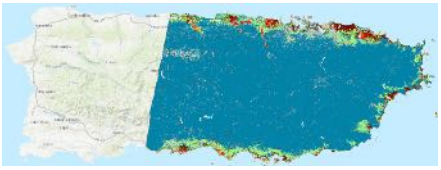

Table A2. *Cont.*

Date	Kappa	User Accuracy for Flooding	Producer Accuracy for Flooding	Overall Accuracy	SAR Image Coverage
31 July 2020 (after a big rainfall event)	0.95	1	0.98	0.96	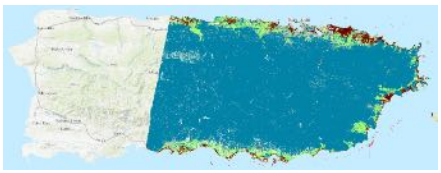
19 September 2022 (Fiona)	0.93	1	1	0.94	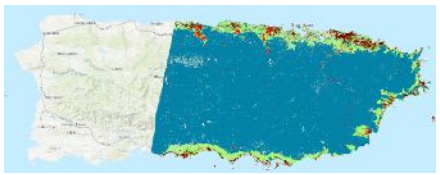
6 November 2022 (after a big rainfall event)	0.95	1	0.99	0.96	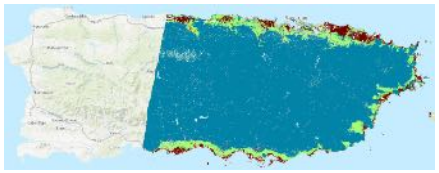

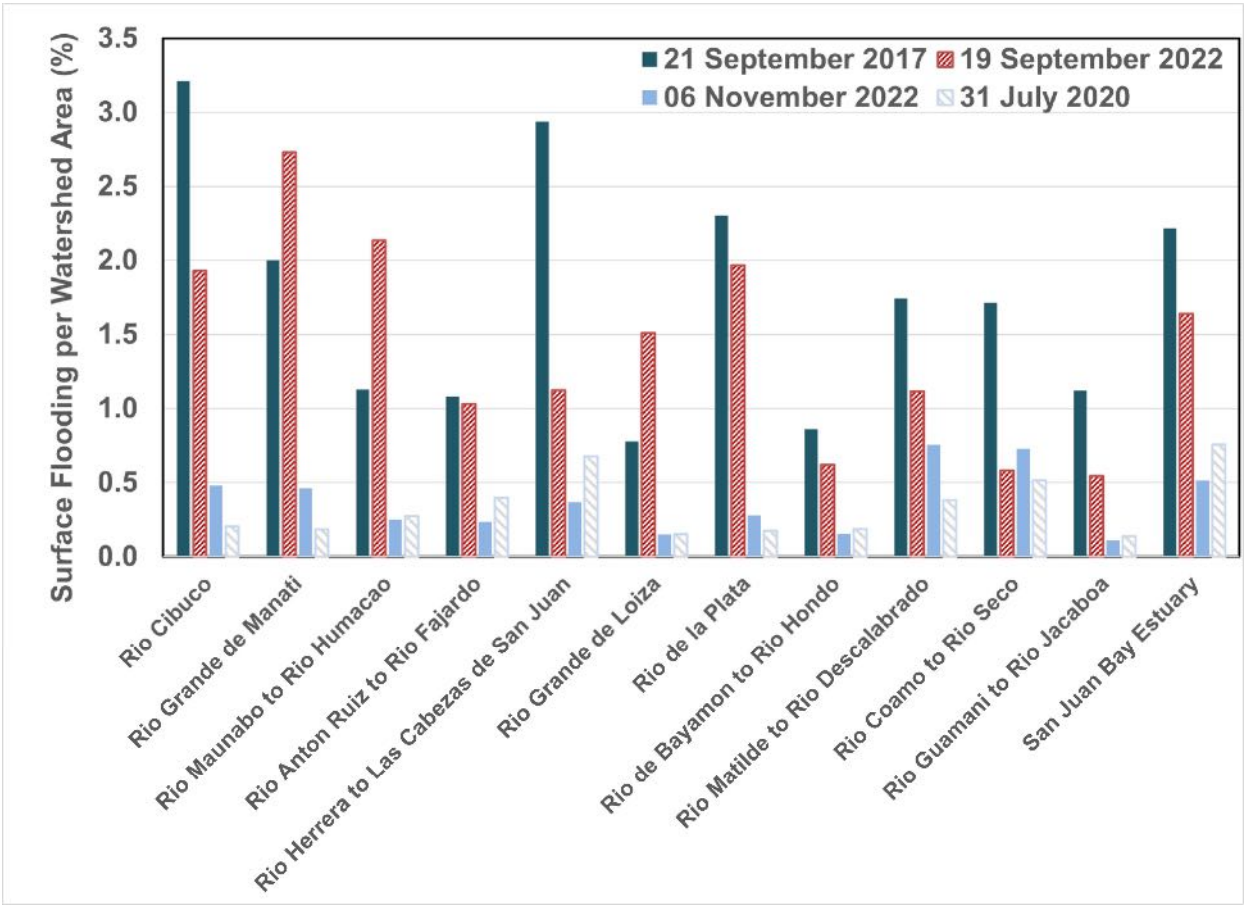

Figure A1. Surface inundation per watershed area (%) detected along coastal watersheds. The events on 21 September 2017 and 19 September 2022 correspond to the flooding after Hurricane Maria (20 September 2017) and Hurricane Fiona (18 September 2022), respectively.

References

1. USGCRP. *Fifth National Climate Assessment*; U.S. Global Change Research Program: Washington, DC, USA, 2023.
2. Cai, W.J.; Wang, G.J.; Santoso, A.; McPhaden, M.J.; Wu, L.X.; Jin, F.F.; Timmermann, A.; Collins, M.; Vecchi, G.; Lengaigne, M.; et al. Increased frequency of extreme La Nina events under greenhouse warming. *Nat. Clim. Chang.* **2015**, *5*, 132–137. [CrossRef]
3. Cai, W.J.; Borlace, S.; Lengaigne, M.; van Rensch, P.; Collins, M.; Vecchi, G.; Timmermann, A.; Santoso, A.; McPhaden, M.J.; Wu, L.X.; et al. Increasing frequency of extreme El Nino events due to greenhouse warming. *Nat. Clim. Chang.* **2014**, *4*, 111–116. [CrossRef]
4. Sippo, J.Z.; Lovelock, C.E.; Santos, I.R.; Sanders, C.J.; Maher, D.T. Mangrove mortality in a changing climate: An overview. *Estuar. Coast. Shelf Sci.* **2018**, *215*, 241–249. [CrossRef]
5. Duke, N.C.; Kovacs, J.M.; Griffiths, A.D.; Preece, L.; Hill, D.J.E.; van Oosterzee, P.; Mackenzie, J.; Morning, H.S.; Burrows, D. Large-scale dieback of mangroves in Australia's Gulf of Carpentaria: A severe ecosystem response, coincidental with an unusually extreme weather event. *Mar. Freshw. Res.* **2017**, *68*, 1816–1829. [CrossRef]
6. Hauer, M.E.; Fussell, E.; Mueller, V.; Burkett, M.; Call, M.; Abel, K.; McLeman, R.; Wrathall, D. Sea-level rise and human migration. *Nat. Rev. Earth Environ.* **2020**, *1*, 28–39. [CrossRef]
7. Neumann, B.; Vafeidis, A.T.; Zimmermann, J.; Nicholls, R.J. Future Coastal Population Growth and Exposure to Sea-Level Rise and Coastal Flooding—A Global Assessment. *PLoS ONE* **2015**, *10*, e0118571. [CrossRef] [PubMed]
8. Uriarte, M.; Thompson, J.; Zimmerman, J.K. Hurricane María tripled stem breaks and doubled tree mortality relative to other major storms. *Nat. Commun.* **2019**, *10*, 1362. [CrossRef]
9. Yu, M.; Gao, Q. Prolonged coastal inundation detected with synthetic aperture radar significantly retarded functional recovery of mangroves after major hurricanes. *Landsc. Ecol.* **2023**, *38*, 169–183. [CrossRef]
10. Patrick, C.J.; Yeager, L.; Armitage, A.R.; Carvallo, F.; Congdon, V.M.; Dunton, K.H.; Fisher, M.; Hardison, A.K.; Hogan, J.D.; Hosen, J.; et al. A System Level Analysis of Coastal Ecosystem Responses to Hurricane Impacts. *Estuaries Coasts* **2020**, *43*, 943–959. [CrossRef]
11. Ye, F.; Huang, W.; Zhang, Y.J.; Moghimi, S.; Myers, E.; Pe'eri, S.; Yu, H.C. A cross-scale study for compound flooding processes during Hurricane Florence. *Nat. Hazards Earth Syst. Sci.* **2021**, *21*, 1703–1719. [CrossRef]
12. Gori, A.; Lin, N.; Xi, D.; Emanuel, K. Tropical cyclone climatology change greatly exacerbates US extreme rainfall–surge hazard. *Nat. Clim. Chang.* **2022**, *12*, 171–178. [CrossRef]
13. Teng, J.; Jakeman, A.J.; Vaze, J.; Croke, B.F.W.; Dutta, D.; Kim, S. Flood inundation modelling: A review of methods, recent advances and uncertainty analysis. *Environ. Model. Softw.* **2017**, *90*, 201–216. [CrossRef]
14. Huang, C.; Chen, Y.; Zhang, S.; Wu, J. Detecting, Extracting, and Monitoring Surface Water from Space Using Optical Sensors: A Review. *Rev. Geophys.* **2018**, *56*, 333–360. [CrossRef]
15. Heimhuber, V.; Tulbure, M.G.; Broich, M. Modeling multidecadal surface water inundation dynamics and key drivers on large river basin scale using multiple time series of Earth-observation and river flow data. *Water Resour. Res.* **2017**, *53*, 1251–1269. [CrossRef]
16. DeVries, B.; Huang, C.; Armston, J.; Huang, W.; Jones, J.W.; Lang, M.W. Rapid and robust monitoring of flood events using Sentinel-1 and Landsat data on the Google Earth Engine. *Remote Sens. Environ.* **2020**, *240*, 111664. [CrossRef]
17. Wulder, M.A.; Loveland, T.R.; Roy, D.P.; Crawford, C.J.; Masek, J.G.; Woodcock, C.E.; Allen, R.G.; Anderson, M.C.; Belward, A.S.; Cohen, W.B.; et al. Current status of Landsat program, science, and applications. *Remote Sens. Environ.* **2019**, *225*, 127–147. [CrossRef]
18. Pahlevan, N.; Chittimalli, S.K.; Balasubramanian, S.V.; Vellucci, V. Sentinel-2/Landsat-8 product consistency and implications for monitoring aquatic systems. *Remote Sens. Environ.* **2019**, *220*, 19–29. [CrossRef]
19. Torres, R.; Snoeij, P.; Geudtner, D.; Bibby, D.; Davidson, M.; Attema, E.; Potin, P.; Rommen, B.; Floury, N.; Brown, M.; et al. GMES Sentinel-1 mission. *Remote Sens. Environ.* **2012**, *120*, 9–24. [CrossRef]
20. Jiang, X.; Liang, S.; He, X.; Ziegler, A.D.; Lin, P.; Pan, M.; Wang, D.; Zou, J.; Hao, D.; Mao, G.; et al. Rapid and large-scale mapping of flood inundation via integrating spaceborne synthetic aperture radar imagery with unsupervised deep learning. *ISPRS J. Photogramm. Remote Sens.* **2021**, *178*, 36–50. [CrossRef]
21. Gorelick, N.; Hancher, M.; Dixon, M.; Ilyushchenko, S.; Thau, D.; Moore, R. Google Earth Engine: Planetary-scale geospatial analysis for everyone. *Remote Sens. Environ.* **2017**, *202*, 18–27. [CrossRef]
22. Liang, J.; Liu, D. A local thresholding approach to flood water delineation using Sentinel-1 SAR imagery. *ISPRS J. Photogramm. Remote Sens.* **2020**, *159*, 53–62. [CrossRef]
23. Shen, X.; Wang, D.; Mao, K.; Anagnostou, E.; Hong, Y. Inundation Extent Mapping by Synthetic Aperture Radar: A Review. *Remote Sens.* **2019**, *11*, 879. [CrossRef]
24. Cian, F.; Marconcini, M.; Ceccato, P. Normalized Difference Flood Index for rapid flood mapping: Taking advantage of EO big data. *Remote Sens. Environ.* **2018**, *209*, 712–730. [CrossRef]
25. Clement, M.A.; Kilsby, C.G.; Moore, P. Multi-temporal synthetic aperture radar flood mapping using change detection. *J. Flood Risk Manag.* **2018**, *11*, 152–168. [CrossRef]
26. Zhan, P.; Zhu, W.; Li, N. An automated rice mapping method based on flooding signals in synthetic aperture radar time series. *Remote Sens. Environ.* **2021**, *252*, 112112. [CrossRef]

27. Huang, W.; DeVries, B.; Huang, C.; Lang, M.W.; Jones, J.W.; Creed, I.F.; Carroll, M.L. Automated Extraction of Surface Water Extent from Sentinel-1 Data. *Remote Sens.* **2018**, *10*, 797. [CrossRef]
28. Leauthaud, C.; Belaud, G.; Duvail, S.; Moussa, R.; Grünberger, O.; Albergel, J. Characterizing floods in the poorly gauged wetlands of the Tana River Delta, Kenya, using a water balance model and satellite data. *Hydrol. Earth Syst. Sci.* **2013**, *17*, 3059–3075. [CrossRef]
29. Ogilvie, A.; Belaud, G.; Delenne, C.; Bailly, J.-S.; Bader, J.-C.; Oleksiak, A.; Ferry, L.; Martin, D. Decadal monitoring of the Niger Inner Delta flood dynamics using MODIS optical data. *J. Hydrol.* **2015**, *523*, 368–383. [CrossRef]
30. López-Marrero, T.; Heartsill-Scalley, T.; Rivera-López, C.F.; Escalera-García, I.A.; Echevarría-Ramos, M. Broadening Our Understanding of Hurricanes and Forests on the Caribbean Island of Puerto Rico: Where and What Should We Study Now? *Forests* **2019**, *10*, 710. [CrossRef]
31. Pasch, R.J.; Penny, A.B.; Berg, R. *National Hurricane Center Tropical Cyclone Report: Hurricane Maria*; (AL152017); National Hurricane Center: Miami, FL, USA, 2019; pp. 1–48.
32. Pasch, R.J.; Reinhart, B.J.; Alaka, L. *National Hurricane Center Tropical Cyclone Report Hurricane Fiona*; (AL072022); National Hurricane Center: Miami, FL, USA, 2023; p. 60.
33. NOAA National Centers for Environmental Information (NCEI). U.S. Billion-Dollar Weather and Climate Disasters. 2023. Available online: https://www.ncei.noaa.gov/access/metadata/landing-page/bin/iso?id=gov.noaa.nodc:0209268 (accessed on 10 January 2024).
34. Hoekman, D.H.; Reiche, J. Multi-model radiometric slope correction of SAR images of complex terrain using a two-stage semi-empirical approach. *Remote Sens. Environ.* **2015**, *156*, 1–10. [CrossRef]
35. Vollrath, A.; Mullissa, A.; Reiche, J. Angular-Based Radiometric Slope Correction for Sentinel-1 on Google Earth Engine. *Remote Sens.* **2020**, *12*, 1867. [CrossRef]
36. Breiman, L. Random Forests. *Mach. Learn.* **2001**, *45*, 5–32. [CrossRef]
37. Office for Coastal Management. *C-CAP Land Cover, Puerto Rico, 2010*; NOAA Office for Coastal Management: North Charleston, SC, USA, 2020.
38. Yu, M.; Gao, Q. Topography, drainage capability, and legacy of drought differentiate tropical ecosystem response to and recovery from major hurricanes. *Environ. Res. Lett.* **2020**, *15*, 104046. [CrossRef]
39. R Core Team. *R: A Language and Environment for Statistical Computing*; R Core Team: Vienna, Austria, 2020.
40. Yu, M.; Gao, Q.; Gao, C.; Wang, C. Extent of Night Warming and Spatially Heterogeneous Cloudiness Differentiate Temporal Trend of Greenness in Mountainous Tropics in the New Century. *Sci. Rep.* **2017**, *7*, 41256. [CrossRef] [PubMed]
41. Zhu, X.X.; Montazeri, S.; Ali, M.; Hua, Y.; Wang, Y.; Mou, L.; Shi, Y.; Xu, F.; Bamler, R. Deep Learning Meets SAR: Concepts, models, pitfalls, and perspectives. *IEEE Geosci. Remote Sens. Mag.* **2021**, *9*, 143–172. [CrossRef]
42. Kim, J.-W.; Lu, Z.; Jones, J.W.; Shum, C.K.; Lee, H.; Jia, Y. Monitoring Everglades freshwater marsh water level using L-band synthetic aperture radar backscatter. *Remote Sens. Environ.* **2014**, *150*, 66–81. [CrossRef]
43. Sagin, J.; Sizo, A.; Wheater, H.; Jardine, T.D.; Lindenschmidt, K.-E. A water coverage extraction approach to track inundation in the Saskatchewan River Delta, Canada. *Int. J. Remote Sens.* **2015**, *36*, 764–781. [CrossRef]
44. Frazier, P.; Page, K. A reach-scale remote sensing technique to relate wetland inundation to river flow. *River Res. Appl.* **2009**, *25*, 836–849. [CrossRef]
45. Gao, Q.; Yu, M. Canopy Density and Roughness Differentiate Resistance of a Tropical Dry Forest to Major Hurricane Damage. *Remote Sens.* **2021**, *13*, 2262. [CrossRef]
46. Garner, A.J. Observed increases in North Atlantic tropical cyclone peak intensification rates. *Sci. Rep.* **2023**, *13*, 16299. [CrossRef]

Disclaimer/Publisher's Note: The statements, opinions and data contained in all publications are solely those of the individual author(s) and contributor(s) and not of MDPI and/or the editor(s). MDPI and/or the editor(s) disclaim responsibility for any injury to people or property resulting from any ideas, methods, instructions or products referred to in the content.